Available online at www.sciencedirect.com

ScienceDirect

MATTER AND RADIATION AT EXTREMES

Matter and Radiation at Extremes xx (2017) 1–12

www.journals.elsevier.com/matter-and-radiation-at-extremes

Review article

In situ determination of crystal structure and chemistry of minerals at Earth's deep lower mantle conditions

Hongsheng Yuan*, Li Zhang

Center for High Pressure Science and Technology Advanced Research, Shanghai, 201203, PR China

Received 10 October 2016; revised 29 December 2016; accepted 24 January 2017
Available online ■ ■ ■

Abstract

Recent advances in experimental techniques and data processing allow in situ determination of mineral crystal structure and chemistry up to Mbar pressures in a laser-heated diamond anvil cell (DAC), providing the fundamental information of the mineralogical constitution of our Earth's interior. This work highlights several recent breakthroughs in the field of high-pressure mineral crystallography, including the stability of bridgmanite, the single-crystal structure studies of post-perovskite and H-phase as well as the identification of hydrous minerals and iron oxides in the deep lower mantle. The future development of high-pressure crystallography is also discussed.

PACS Codes: 74.62.Fj; 07.85.Qe; 61.05.C; 81.30.t; 81.10.h

Keywords: X-ray diffraction; Multigrain; Lower mantle; High pressure-temperature

1. Introduction

Pressure, temperature and chemical composition ($P-T-X$) determine the phase diagrams, accounting for the material diversity of nature. These three dimensions are strongly correlated in geophysical and geochemical studies. Our knowledge of Earth's constitution is built on experimental measurements and theoretical simulations of the physical properties of minerals at high $P-T$ conditions in comparison with seismic models [1,2]. Of all the properties, crystal structure and chemistry provide fundamental information, such as atomic arrangement and elemental partitioning of individual minerals in deep Earth.

Accurate determination of high-pressure mineral structure is crucial for understanding all other pressure-induced property changes in the deep Earth. Polycrystalline structural refinement provides limited information about crystal structure, and single-crystal X-ray diffraction (XRD) will be the ideal method for structural determination. However, crystallography under deep-Earth conditions has been limited to polycrystalline samples because single crystals are unachievable in phase transition studies at ultrahigh pressures. This problem has been overcome by sorting out hundreds of submicron crystallites, and refining the structure of several selected crystallites [3,4].

2. Crystal structure and chemistry of silicates in the D″ region

At a depth of ~2890 km in the Earth's deep interior, the slowly convecting, highly viscous mantle silicates meet the liquid metals of the outer core. A thermal boundary is generated at the core-mantle boundary (CMB) where the temperature steeply increases to nearly 4000 K at the boundary of the core [5]. Seismic observations show that

* Corresponding author.
E-mail address: hongsheng.yuan@hpstar.ac.cn (H.S. Yuan).
Peer review under responsibility of Science and Technology Information Center, China Academy of Engineering Physics.

http://dx.doi.org/10.1016/j.mre.2017.01.002

Please cite this article in press as: H. Yuan, L. Zhang, In situ determination of crystal structure and chemistry of minerals at Earth's deep lower mantle conditions, Matter and Radiation at Extremes (2017), http://dx.doi.org/10.1016/j.mre.2017.01.002

approximately 100–350 km above the core-mantle boundary, the so-called D″ layer presents a number of enigmatic features. These seismic anomalies in the D″ boundary include the D″ discontinuity, S wave polarization anisotropy, anticorrelated seismic velocity anomalies, and ultralow velocity zones (ULVZ) [6,7]. Sidorin et al. speculated that several intriguing seismic observation in the D″ layer can be explained by a solid–solid phase transition with a positive P/T slope of the boundary (Clapeyron slope) [8]. In 2004, Murakami et al. discovered the bridgmanite to post-perovskite transition in magnesium silicate ($MgSiO_3$), the dominant mineral in Earth's mantle [9]. Many significant predictions and experimental results have been achieved on this phase transition by the geological community, providing one valid interpretation of the seismological observations in the D″ region. However, recent observations of several abrupt increases in seismic velocity cannot be explained by a simple model of an isochemical $MgSiO_3$ phase transition from bridgmanite to post-perovskite, suggesting the possibility of compositional variations in the deep mantle [10].

2.1. Structural changes through bridgmanite to post-perovskite transition

The phase transition from bridgmanite to post-perovskite was observed experimentally in a polycrystalline sample above 125 GPa and 2500 K in a laser-heated DAC, as shown in Fig. 1 [9]. Here, we focus on the crystal structure and chemistry of bridgmanite and post-perovskite, the two dominant minerals in the lower mantle. The powder diffraction pattern alone did not allow unambiguous structure determination of the newly observed phase. The crystal structure of the post-perovskite was then predicted by theoretical calculations, which revealed the $CaIrO_3$-type structure with space group *Cmcm* [9,11,12].

$CaIrO_3$-type $MgSiO_3$ post-perovskite adopts a 2D structure with edge- and corner-sharing SiO_6 octahedra arranged in linear chains along *a* and *c* axes, respectively (see Fig. 2). These edge- and corner-sharing SiO_6 octahedra sheets are alternated with interlayer Mg^{2+} ions along *b* axis (see Fig. 2). However, $MgSiO_3$ bridgmanite crystallizes in a 3D network structure with only corner-sharing SiO_6 octahedra. Because of the fundamental differences in crystal structures between bridgmanite and $CaIrO_3$-type post-perovskite phases, first-principle calculations have predicted that the bridgmanite to post-perovskite transition has extraordinary property changes that may account for the large seismic anomalies observed in the D″ region [11].

Existing models of a bridgmanite dominant lower mantle have been built on the assumption that the atomic ratio Fe/(Fe + Mg) is nearly 0.1 in the entire lower mantle and a small percent of Al_2O_3 can be incorporated into the silicate phase [2]. The most abundant silicate mineral in Earth is Mg-silicate bridgmanite with 5–10 mol% of Fe and Al existing from 660-km depth to the D″ region. Bridgmanite can be synthesized above 20 GPa and ~1000 K in a multianvil apparatus and single crystals with a size of 10–100 μm can be recovered to ambient

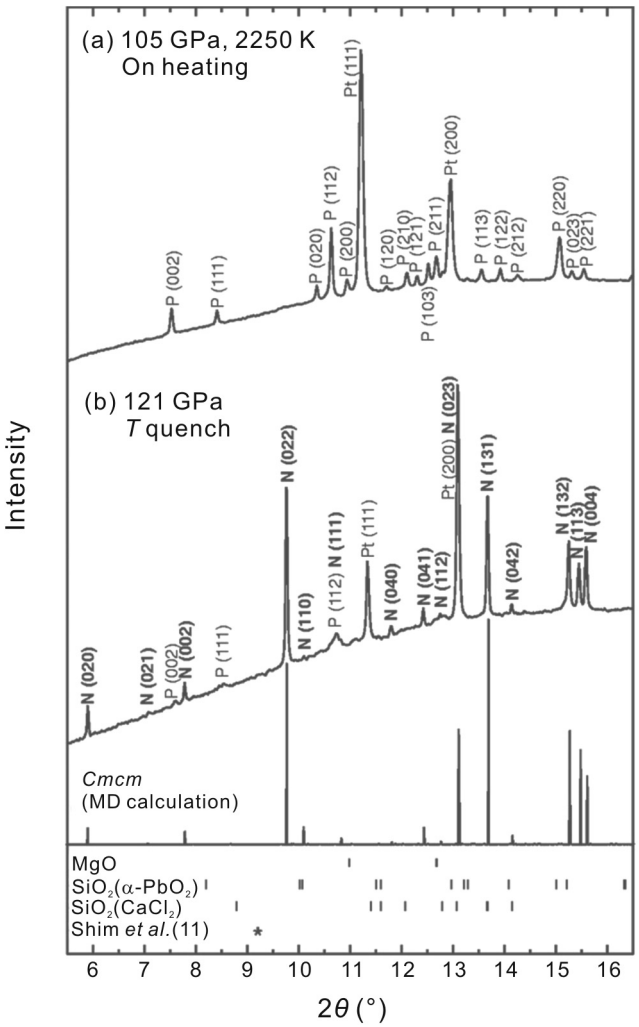

Fig. 1. XRD patterns of $MgSiO_3$ at (a) 105 GPa and 2250 K, (b) 121 GPa and 300 K after heating at 127 GPa [9]. Definitions are P, *Pbnm* perovskite; Pt, platinum; N, new phase (post-perovskite). The calculated powder XRD pattern of the post-perovskite is shown for comparison. The small ticks indicate the peak positions of MgO and both α-PbO_2-type and $CaCl_2$-type SiO_2.

conditions for detailed structural studies. As a result, the effects of Fe^{2+}, Fe^{3+} and Al^{3+} on the bridgmanite have been extensively studied by various research groups [13–18]. In contrast, post-perovskite structure is unquenchable, and in-situ high $P–T$ XRD experiments are essential to understand the structure–property relation [19–21]. Seismological observations show that the depth extent (or sharpness) of the D″ seismic velocity discontinuity is less than 75-km, corresponding to the pressure of <4 GPa [22–24]. However, in-situ high $P–T$ experiments find that substitution of Fe and Al in $MgSiO_3$ bridgmanite tends to expand the transition over a much broader pressure range [25]. Considering strong thermal and chemical heterogeneities in the D″ layer, improved constraints from both seismology and mineral physics are needed [22].

Interestingly, interaction between the lowermost mantle and the liquid outer core may lead to an increased incorporation of Fe content into the D″ region [26,27]. Yamanaka et al. performed powder XRD Rietveld analysis on Fe-rich ($Mg_{0.6}Fe_{0.4}$)SiO_3 post-perovskite, suggesting a structure with the *Pmcm*

Please cite this article in press as: H. Yuan, L. Zhang, In situ determination of crystal structure and chemistry of minerals at Earth's deep lower mantle conditions, Matter and Radiation at Extremes (2017), http://dx.doi.org/10.1016/j.mre.2017.01.002

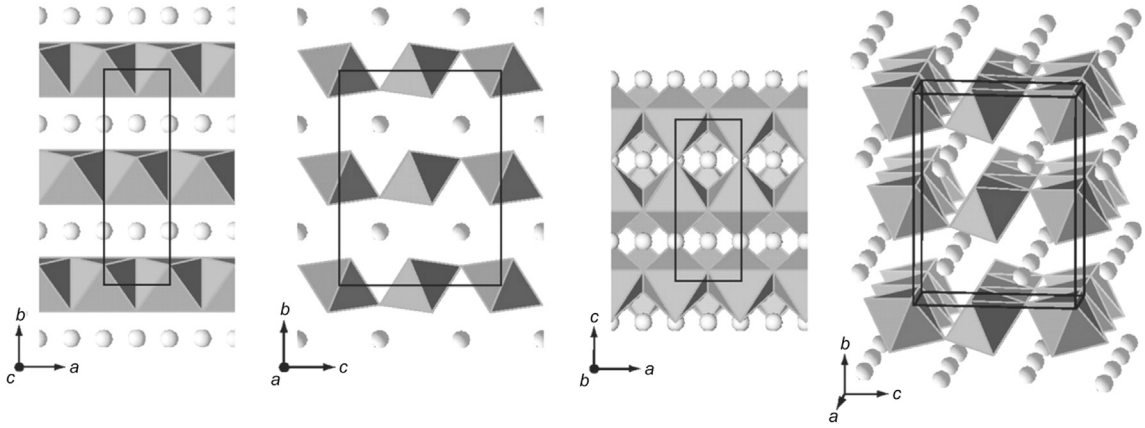

Fig. 2. Crystal structure of the post-perovskite phase projected along [001], [100], and [010] directions and a stereoscopic view showing the layer stacking structure, respectively [9]. Coordination polyhedra of oxygen atoms around Si atoms are shown as octahedra, and Mg^{2+} ions are shown as spheres.

(*Pmma*) space group, indicative of a subtle structural change in post-perovskite due to Fe-enrichment [28]. In general, the post-perovskite structure determined by Rietveld powder diffraction refinements at extreme $P-T$ conditions suffers from unreliable intensity measurements caused by texturing of the sample and/or speckled diffraction patterns derived from crystal growth under high T. For the latter, although the speckled XRD patterns are not compatible with either powder or conventional single-crystal structural refinements, a unique analytical approach known as multigrain crystallography has been successfully developed for the structure solution of a multigrain sample [29].

2.2. Single-crystal determination of (Mg, Fe)SiO_3 post-perovskite via multigrain crystallography

Precise measurement of the crystal structure of post-perovskite at extreme conditions corresponding to the D″ region is highly desired to provide direct and fundamental testing for the predicted unusual property changes across the bridgmanite to post-perovskite transition. However, it is technically infeasible to prepare a suitable single-crystal post-perovskite sample for conventional single-crystal XRD analysis. The first single-crystal structure model of Fe-bearing post-perovskite has been evaluated via multigrain crystallography, providing a reliable reference for structural studies using other approaches [3]. Here, preparation of a good quality sample is the most essential and critical step for the multigrain analysis; however, there are many aspects of the necessity for continuous exploration and practice, such as hydrostatic conditions, sample and heating homogeneity, and the kinetics process involved in phase transitions. After numerous trials, it was found that the high-quality post-perovskite samples for single-crystal determination could be meticulously prepared as follows. First, a single-crystal orthopyroxene sample with a composition of $(Mg_{0.85}Fe_{0.15})SiO_3$ was pre-compressed into a disk of ~10 μm thickness cut to 40–60 μm in diameter, and then placed in a ~60 μm diameter Re gasket hole in a Mao-type symmetric DAC for each experiment. Thus, sample homogeneity and non-porosity was ensured. No additional laser absorber is needed, because the sample itself can well absorb the laser, which builds a solid support for uniform heating. Secondly, compressed Ne was loaded, and the sample was successfully sandwiched between symmetric Ne layers from both sides. Here, Ne was served as the pressure transmitting medium to provide quasi-hydrostatic pressure, as the Vinet pressure scale to ensure pressure consistency with the well-accepted Au scale [30,31], and as the thermal insulation layer during laser heating for reaching phase equilibrium. The as-prepared sample was initially compressed to 109 GPa at room temperature and then heated directly to 2200–2400 K. It was found that the post-perovskite phase appeared as a minor phase compared to the bridgmanite and the pressure increased to 111 GPa after T quenching. Then, $P-T$ conditions were increased to 118 GPa at 2300–2500 K where the post-perovskite became the dominant phase. After T quenching (pressure was increased to 120 GPa), the XRD pattern showed discrete spots instead of continuous Debye rings (see Fig. 3), indicating the formation of a coarse-grained multigrain aggregate.

Similar to the "rotation method" used in conventional single-crystal crystallography, diffraction patterns were collected in step-scans (2 s/step) with both 0.2° and 1.0° rotation steps over the range of ω from −26.6° to 24.6° at 120 GPa. Proper exposure time should be applied to ensure the high signal/background ratio of diffractions, and in the meantime prevent the peak intensity exceeding the over-saturation point of the detector. Diffraction spots from the coarse polycrystalline sample comprised of up to hundreds of individual submicron crystals can be recorded using the high brilliance monochromatic X-ray beam with a beam size of 6 μm × 8 μm at HPCAT, APS. The Fully Automatic Beam-Line Experiments (FABLE) package was used to process and index diffraction spots, and the orientation matrices of individual grains were indexed using the GrainSpotter algorithm [32]. The set of peaks corresponding to one crystallite, identified by FABLE, was exported into GSE_ADA/RSV software package [33], where peak fitting was performed and

Please cite this article in press as: H. Yuan, L. Zhang, In situ determination of crystal structure and chemistry of minerals at Earth's deep lower mantle conditions, Matter and Radiation at Extremes (2017), http://dx.doi.org/10.1016/j.mre.2017.01.002

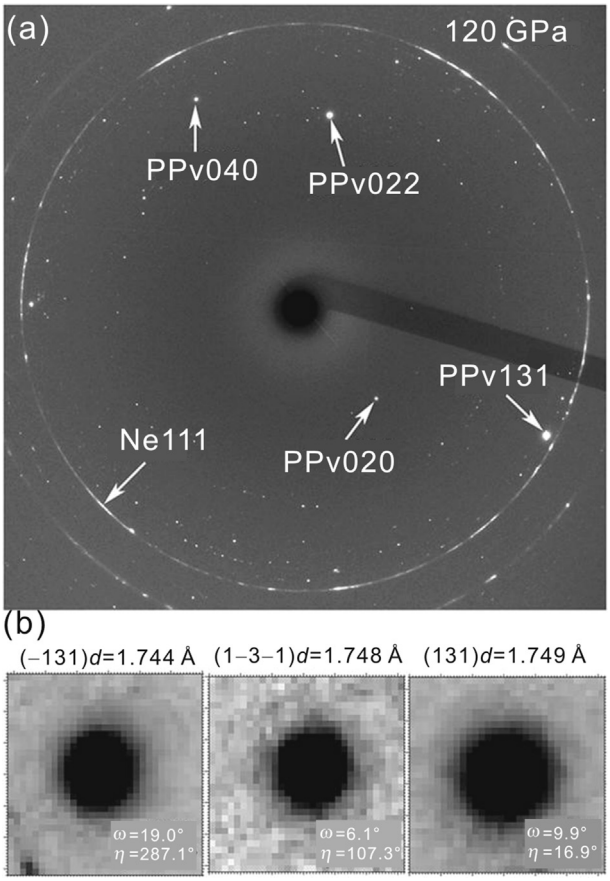

Fig. 3. Powder diffraction patterns of (Mg, Fe)SiO_3 post-perovskite at 120 GPa and after T quenching [3]. (a) A representative speckled XRD pattern of the post-perovskite sample at a fixed ω angle; (b) ROI images of three {131} diffraction spots from one selected single crystallite of the post-perovskite phase.

appropriate corrections accounting for Lorenz, polarization, DAC absorption, and sample motion effects were applied. In these experiments, the crystal size in a multigrain sample was typically a few hundred nm while the beam size (5−10 μm in diameter) was about one order of magnitude larger than the crystal size, which means a big portion of the grains could bathe within the X-ray during the sample rotation. In this case, the effects of sample absorption and rotation could be minimized. Structural refinements were carried out using SHELXL97 [34].

The single-crystal diffraction pattern was indexed with the $CaIrO_3$-type post-perovskite structure: a = 2.466 (1) Å, b = 8.130 (6) Å, c = 6.108 (10) Å. Listed in Table 1 are selected lattice parameters, bond lengths and interatomic angles in the structure of post-perovskite at high P and room temperature in comparison with the results from powder diffraction data in $(Mg_{1-x},Fe_x)SiO_3$ ($0 \le x \le 0.1$). The Fe content in the post-perovskite phase was refined to $x = 0.07$ when the Fe-Mg ratio was used as a variable in the refinement. The obtained structural parameters in Fe-bearing post-perovskite are consistent with Fe-free post-perovskite from the theoretically calculated structural mode, suggesting that the Fe content in the mantle has a negligible effect on the crystal structure of the post-perovskite phase.

Table 1
Selected lattice parameters, bond lengths (Å) and interatomic angles (°) in the single-crystal post-perovskite structure at 120 GPa and 300 K in comparison with results from previous power diffraction data for $(Mg_{1-x}Fe_x)SiO_3$.

Parameters	Single crystal [3]	Powder [28]	Powder [21]	Theory [9]	Powder [70]
Formula (x)	0.07	0.1	0.09	0	0
P (GPa)	120 (4)	131	126 (2)	121	116
a (Å)	2.466 (1)	2.4597 (7)	2.460 (1)	2.456	2.4687 (5)
b (Å)	8.130 (6)	8.0505 (29)	8.059 (3)	8.042	8.1165 (20)
c (Å)	6.108 (10)	6.1051 (14)	6.102 (2)	6.093	6.1514 (13)
V (Å^3)	122.5 (2)	120.89 (6)	121.0 (1)	120.39	123.26 (3)
Si−O1 × 2	1.63 (2)	1.62	1.66 (1)	1.64	1.61
Si−O2 × 4	1.72 (2)	1.73	1.71 (2)	1.66	1.72
Mg−O1 × 2	1.87 (3)	1.85	1.85 (3)	1.84	1.95
Mg−O2 × 4	1.93 (2)	1.95	1.88 (2)	1.94	1.95
Mg−O2 × 2	2.09 (3)	2.01	2.15 (3)	2.13	2.07
∠SiO1Si	139 (3)	141	134 (2)	138	146
∠SiO2Si	92 (1)	91	92 (2)	94	92

2.3. Disproportionation of (Mg, Fe)SiO_3 bridgmanite in Earth's deep lower mantle

As suggested by Yamanaka et al. [28], if the ultralow-velocity zones at the very base of the lower mantle are highly enriched in Fe from reacting with the outer core, the post-perovskite phase might alter its space group from *Cmcm* to *Pmcm* depending on the degree of Fe enrichment. However, subsequent study found that (Mg, Fe)SiO_3 bridgmanite lost its Fe and disproportionates to a nearly Fe-free $MgSiO_3$ perovskite phase and an Fe-rich phase [4]. Zhang et al. carried out experiments on $(Mg_{0.85}Fe_{0.15})SiO_3$ orthopyroxene sample in laser-heated diamond anvil cells, at a pressure of 94 GPa and temperature of 2300 K [4]. The sample preparation procedure was similar to that in the last section. In addition to bridgmanite, it was found that another set of peaks not corresponding to any previously known phases appeared with particularly conspicuous peaks at 2.55 and 2.40 Å (marked as H110 and H101, respectively in Fig. 4). On the basis of six distinct new peaks at 4.413, 2.549, 2.401, 1.904, 1.471 and 1.441 Å, it can be concluded that this phase has a hexagonal unit cell of a = 5.096 (2) Å and c = 2.862 (3) Å and a molecular volume V = 32.19 (4) Å^3 with formula units per unit cell $Z = 2$, referred to as H-phase. The molar volume of the H-phase was slightly larger than that of the coexisting bridgmanite. Coexisting $MgSiO_3$ bridgmanite and H-phase coarse-grained multiple-crystal aggregate can be synthesized at 101 GPa in another experiment (see Fig. 5), indicating that the H-phase is reproducible. Then multigrain analysis was used to identify H-phase and bridgmanite and to constrain their unit cells. It is of importance that the phase H was unambiguously detected in separate experiments at pressures of 85−101 GPa, temperatures of 2200−2400 K for samples with the composition of $(Mg_{0.60}Fe_{0.40})SiO_3$, $(Mg_{0.90}Fe_{0.10})SiO_3$ and $(Mg_{0.80}Fe_{0.20})(Al_{0.04}Si_{0.96})O_3$. All the starting samples were synthesized by the well-established synthesis procedure described in earlier studies [35]. In particular, the $(Mg_{0.90}Fe_{0.10})SiO_3$ sample was from the same batch that has been used in previous studies [36,37].

Please cite this article in press as: H. Yuan, L. Zhang, In situ determination of crystal structure and chemistry of minerals at Earth's deep lower mantle conditions, Matter and Radiation at Extremes (2017), http://dx.doi.org/10.1016/j.mre.2017.01.002

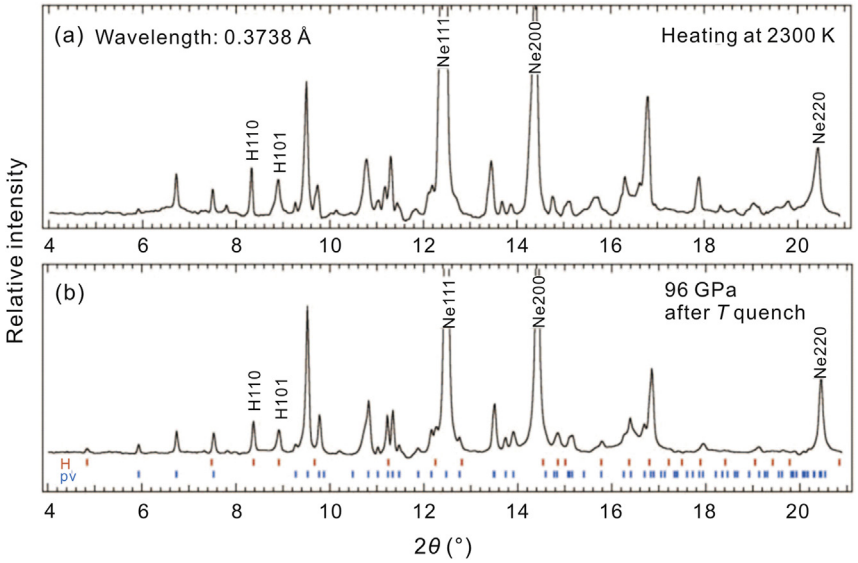

Fig. 4. In situ powder XRD patterns of $Mg_{0.85}Fe_{0.15}SiO_3$ in Ne medium [4]. Coexistence of bridgmanite phase (or Pv) and H-phase (a) during laser-heating at 2300 K and (b) after T quench to 300 K and 96 GPa. Because of the multigrain speckled nature of the patterns, the relative peak intensities are affected by the presence or absence of strong spots. The peak at d ~2.7 Å, which is 7.8° in (b), belongs to a small amount of SiO_2 ($CaCl_2$ structure) added to the starting material.

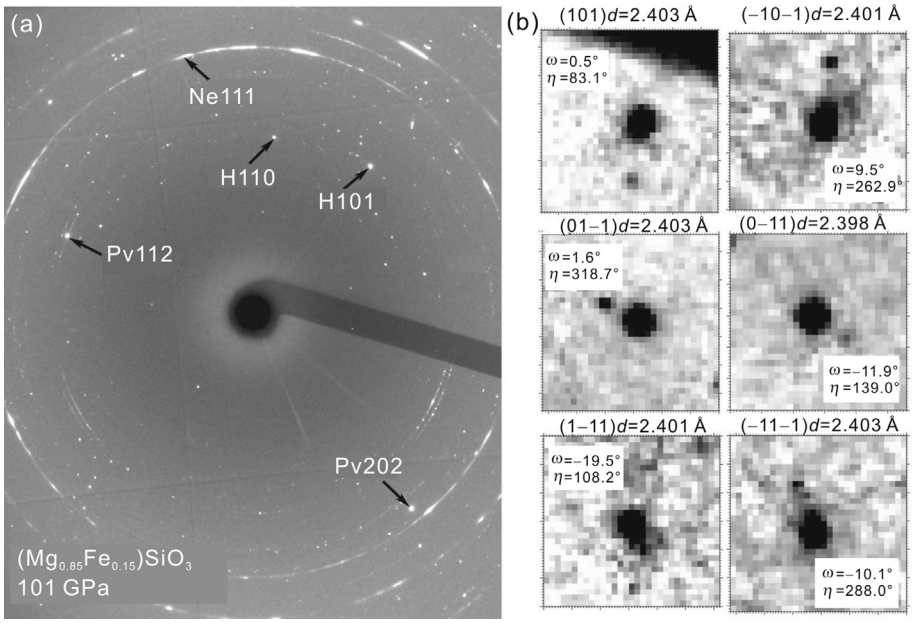

Fig. 5. Selection of $MgSiO_3$ bridgmanite (or Pv) and H-phase individual single crystals using the multigrain method [4]. (a) A representative speckled multiple-crystal XRD pattern of the H-phase and coexisting bridgmanite in $Mg_{0.85}Fe_{0.15}SiO_3$ at 101 GPa and after T quench (X-ray wavelength of 0.3738 Å), and the marked Miller indices show some of the most intense diffraction spots. (b) Six {101} diffraction reflections at different rotation angle ω and azimuthal angle η belonging to one selected crystallite of H-phase at 101 GPa.

The combination of focused ion beam (FIB) with scanning transmission electron microscopy (STEM) techniques together with energy-dispersive X-ray (EDX) analysis has been used to analyze the chemical compositions of samples recovered from a laser-heated DAC [38–41]. The STEM-EDX compositional mapping results showed that the composition and structure of the quenched bridgmanite matched the XRD data of the same bridgmanite quenched to ambient conditions, confirming Fe depletion in bridgmanite as a result of disproportionation (see Fig. 6). The H-phase related amorphous product was highly unstable under ambient conditions and further decomposed during the sample preparation process for STEM (see Fig. 6, positions 3 and 4). The Fe enrichment in H-phase was confirmed with EDX at ambient conditions. It can be concluded that (Mg, Fe)SiO_3 loses its Fe and breaks down to a nearly Fe-free $MgSiO_3$ bridgmanite phase and an Fe-rich phase with a hexagonal structure. The breakdown will change the composition of mantle minerals, likely affecting

Please cite this article in press as: H. Yuan, L. Zhang, In situ determination of crystal structure and chemistry of minerals at Earth's deep lower mantle conditions, Matter and Radiation at Extremes (2017), http://dx.doi.org/10.1016/j.mre.2017.01.002

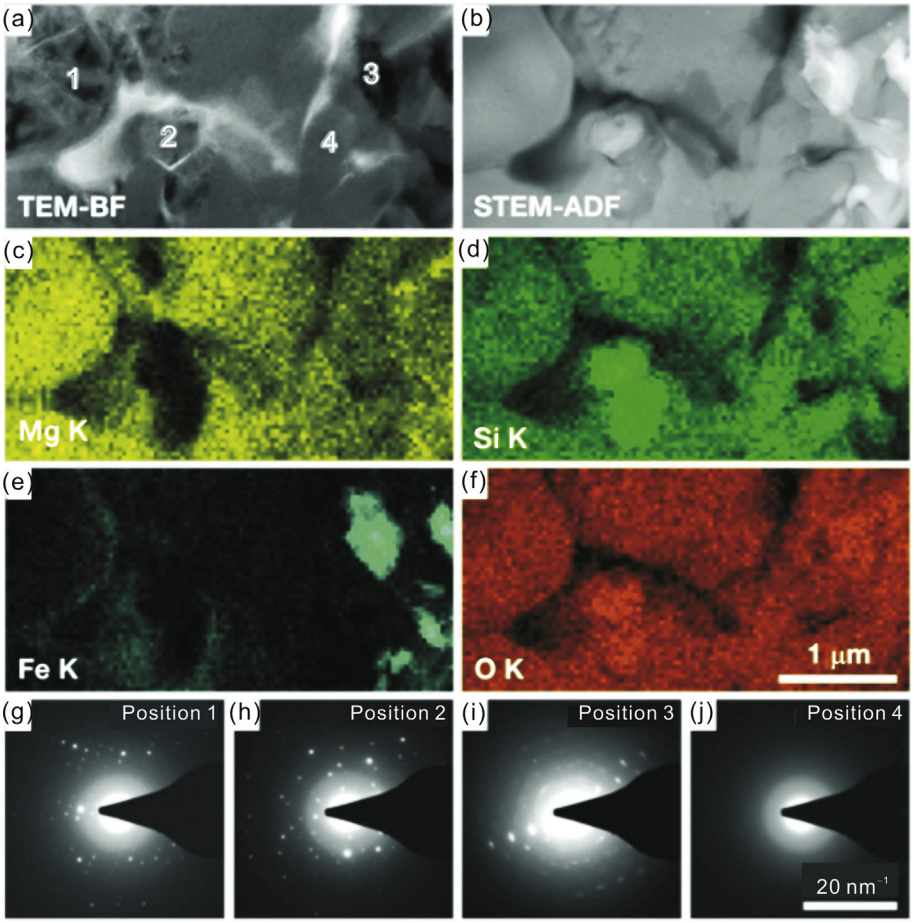

Fig. 6. STEM-EDX analysis of the recovered products [4]. (a) TEM-BF image. (b) STEM-annular dark-field (ADF) image. Corresponding STEM-EDX maps: (c) Mg K, (d) Si K, (e) Fe K, and (f) O K. STEM-ADF and EDX maps are obtained simultaneously. (g)–(j) SAED patterns are obtained from the positions indicated in (a).

the depth and thickness of the bridgmanite to post-perovskite transition, consistent with the argument that the D″ layer may be chemically heterogeneous in previous studies. This observation suggests that the lower mantle may contain previously unidentified major phases, which have implications for enigmatic seismic features beyond ~2000 km depth. Importantly, multigrain analysis of submicron-grained single-crystals can separate the effects from composition, pressure, and/or sample quality on the multiphase samples above Mbar pressure.

3. Hydrous minerals and water storage in the deep lower mantle

The knowledge of water (or hydrogen) recycling and storage in Earth is critical to understand the physical and rheological properties of the mantle [42]. The recent discovery of hydrous ringwoodite as inclusions in ultra deep diamonds from Juina, Brazil suggests significant water capacity of ultramafic rocks in the transition zone [43]. Through the subduction of hydrous minerals in cold slabs, a certain amount of water can be transported into the Earth's deep interior. Seismic tomography images imply that slabs of subducted oceanic lithosphere can sink into the deep lower mantle [44]. Over the last several decades, high pressure studies showed that several dense hydrous magnesium silicates (DHMS phases) in the simplified $MgO–SiO_2–H_2O$ system were thermodynamically stable in peridotites within subducting lithosphere. In the lower mantle, these minerals may exist in the form of $Mg_{10}Si_3O_{14}(OH)_4$ (known as superhydrous phase B or phase C) [45], $MgSi_2O_4(OH)_2$ (known as phase D) [46] and $MgSiO_2(OH)_2$ (known as phase H) [47,48]. However, these Mg–Si endmembers are expected to stabilize only in the cold subducted slabs and to break down at warmer temperatures close to those of typical mantle geotherms or hot subducted slabs. Recent investigations conclude that the incorporation of A_2O_3 stabilizes the hydrous phases at high temperature, forming water reservoirs in deep mantle [42,49,50].

3.1. Hydrous phase H–δ ($MgSiO_2(OH)_2$–AlOOH) solid solutions

Applying in situ XRD measurements in conjunction with a multi-anvil apparatus using sintered diamond anvils, Nishi et al. showed that phase D transformed to an assemblage with hydrous phase H at pressures above 48 GPa [47]. The experimental results are in agreement with the theoretical

Please cite this article in press as: H. Yuan, L. Zhang, In situ determination of crystal structure and chemistry of minerals at Earth's deep lower mantle conditions, Matter and Radiation at Extremes (2017), http://dx.doi.org/10.1016/j.mre.2017.01.002

calculation by Tsuchiya et al. which predicted that phase H had a narrow stability field at pressures of 40–52 GPa and temperature of 0 K [51]. It was reported that hydrous phase H can be reasonably indexed with an orthorhombic symmetry with the space group of *Pnnm* [47]. The neutron powder diffraction analysis suggested that the hydrogen distribution in phase H with the disordered cations would display a fully disordered hydrogen bond pattern [52]. For hydrous δ-AlOOH (phase δ), pressure-induced reversible phase transition from the space group of $P2_1nm$ to *Pnnm* between 6.1 and 8.2 GPa has been confirmed by single-crystal XRD [53]. Several theoretical studies have proposed the possibility of pressure-induced hydrogen bond symmetrization in δ-AlOOH, which possibly accounts for its high thermal stability at extreme conditions [54–57]. However, the O–O distance of hydrogen bond (2.439 (6) Å at 8.2 GPa) determined by single-crystal analysis was significantly longer than the predicted distance (2.366 Å) of the hydrogen bond symmetrization in δ-AlOOH [53]. The pressure-induced phase transition to *Pnnm* symmetry in δ-AlOOH can be explained by the disordered arrangement of hydrogen. Thus, phase H–δ solid solutions with the space group of *Pnnm* can be generated at high pressure conditions.

The orthorhombic δ-AlOOH (*Pnnm*) is stable over the entire range of conditions of the lower mantle, from 33 to 134 GPa at 1350–2300 K [58,59]. In addition, Tsuchiya el al. predicted that δ-AlOOH remained stable up to ~170 GPa, and then transformed to a pyrite-type structure [54]. Considering the substitution mechanism of $2Al^{3+} = Mg^{2+} + Si^{4+}$, Ohira et al. reported the remarkable effect of Al on the thermal stability and chemical partitioning for the phase H–δ ($MgSiO_2(OH)_2$–AlOOH) solid solution under lower mantle conditions [49]. Hydrous gels with the composition of 70 mol % $MgSiO_3$–30 mol% Al_2O_3 were synthesized by the sol–gel method, and the starting samples containing 7.0, 6.0 and 1.5 wt.% H_2O were achieved by controlled heating treatments [49]. The disk of the starting material with the thickness of ~30 μm was sandwiched between two Pt foils and embedded in NaCl or gels as the pressure medium. Pt was used as the laser absorber and pressure standard. Typical XRD patterns of samples with 6.0 wt.% water content showed the coexistence of bridgmanite and phase H–δ at 64 GPa and 2110 K, while a coexisting post-perovskite and phase H–δ assemblage was found at 128 GPa and 2190 K (see Fig. 7) [49]. TEM images coupled with EDX analysis showed that both bridgmanite and post-perovskite in the recovered samples were alumina-depleted with about 5–7 mol% Al_2O_3 (see Fig. 8) [49]. The content of phase δ in bridgmanite and phase H–δ assemblage was about 50–60 mol%, while the content of phase δ in post-perovskite and phase H–δ assemblage was about 70–80 mol %. In short, the reaction between water and aluminous $MgSiO_3$ can form alumina-depleted bridgmanite/post-perovskite and hydrous phase δ–H solid solution, and the latter can further transport water into the region of the core–mantle boundary [49].

Ex situ TEM-EDX analysis provides information on chemical compositions estimation and phase identification, complementary to the information obtained from in situ

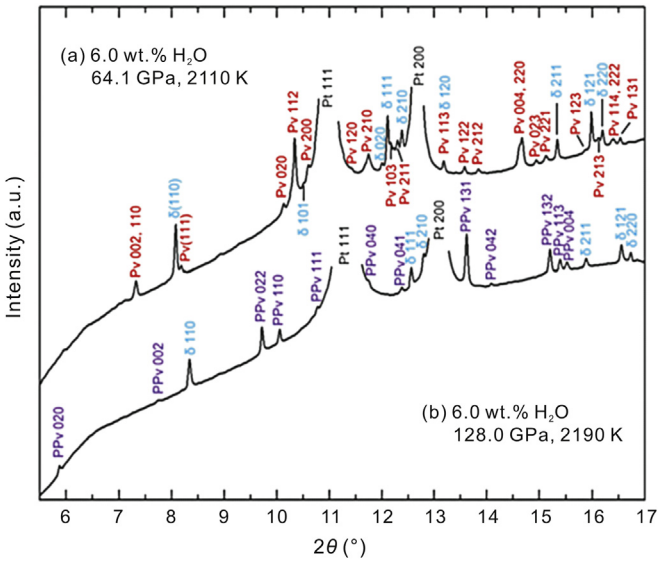

Fig. 7. In situ XRD profiles of the runs conducted at 64.1 GPa and 2110 K, and 128.0 GPa and 2190 K [48]. (a) Coexistence of bridgmanite (or Pv) and hydrous δ-phase AlOOH–$MgSiO_2(OH)_2$ at 64.1 GPa and 2110 K. (b) Coexistence of post-perovskite (PPv) and δ at 128.0 GPa and 2190 K.

powder XRD results at high *P–T*, provided that all the phases and their chemical compositions remain unchanged after *P–T* quench to ambient conditions [4,38–41]. As sinking slabs may deliver a great amount of Al to the lower mantle through Al-rich minerals, further studies in Ca, Fe-bearing aluminous $MgSiO_3$ compositions are needed.

3.2. High thermal stability of Al-phase D–$Al_2SiO_4(OH)_2$

Pamato et al. investigated the phase assemblages of hydrous aluminous silicates with the composition of Al_2O_3:SiO_2 = 2:1 containing 13 wt.% H_2O and Al_2O_3:SiO_2 = 1:1 containing 19 wt.% H_2O in a multi-anvil press at pressures of 18–26 GPa and temperatures of 1000–2100 °C [50]. The as-synthesized samples were characterized by XRD, electron probe microanalysis, TEM and Raman spectroscopy. It was found that Al-phase D, $Al_2SiO_4(OH)_2$ could be synthesized at temperatures extending over 2000 °C at 26 GPa. Raman measurements of this Al-phase D detected the strong hydroxyl vibrational modes, qualitatively confirming a significant hydroxyl concentration [50]. The results indicated that Al-phase D could survive at least in the upper mantle under mantle thermo conditions. The high thermal stability of Al-phase D was assigned to its unique crystal structure. In the crystal structure of Mg-phase D (space group: $P\bar{3}1m$), two separated layers consisting of the SiO_6 and MgO_6 octahedra stacked along the *c* direction with Mg and Si in the 1*a* and 2*d* Wyckoff positions respectively (M1 and M2; see Fig. 9) [50]. Three additional octahedral sites regarding the 2*c* and 1*b* Wyckoff positions (M3 and M4) remained vacant. However, when Al replaced Mg in Al-phase D (space group: $P6_3/mcm$), all six octahedral sites became partially occupied by a random and disordered distribution of Si and Al in equivalent M1/M4 and M2/M3 sites, resulting in a symmetrical increase.

Please cite this article in press as: H. Yuan, L. Zhang, In situ determination of crystal structure and chemistry of minerals at Earth's deep lower mantle conditions, Matter and Radiation at Extremes (2017), http://dx.doi.org/10.1016/j.mre.2017.01.002

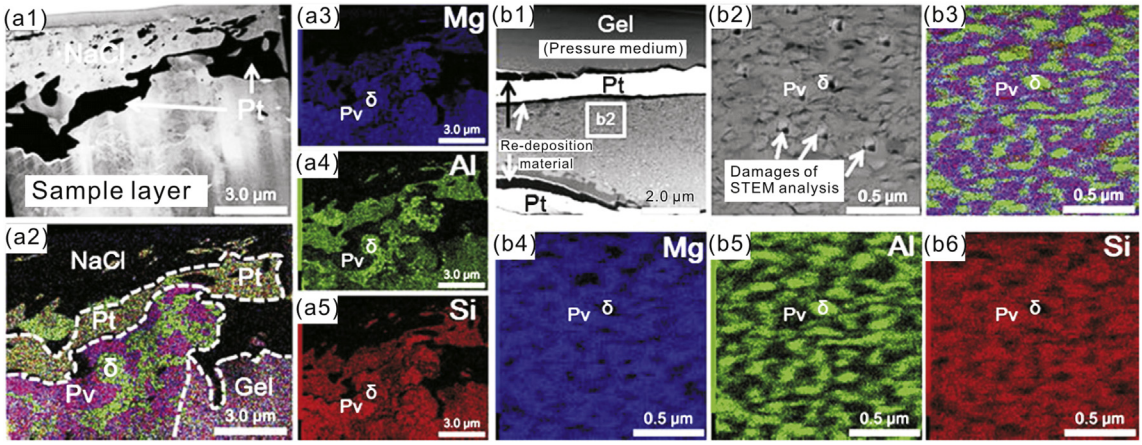

Fig. 8. Elemental mapping images for Mg, Al and Si for samples recovered from high-pressure and high-temperature conditions [48]. (a) TEM images of recovered sample (starting sample with 1.5 wt.% H_2O) from 68 GPa and 2010 K. (a1) Bright field STEM image. (a2) Overlapped Mg+ Al+ Si mapping image. Alumina-depleted bridgmanite (or Pv, purple) and hydrous δ-phase AlOOH−$MgSiO_2(OH)_2$ coexist at the lower left of the image. The signals of Mg, Al, and Si in platinum foil in (a2) are artifact from the peak overlapping of MgKα, AlKα, and SiKα and a large background from large Mα and Mz peaks of Pt. (a3) Mg mapping image, (a4) Al mapping image, and (a5) Si mapping image. (b) TEM images of recovered sample (starting sample with 6.0 wt.% H_2O) from 128 GPa and 2190 K. (b1) dark field STEM image. Fractures were formed between Pt and silicate minerals during decompression. (b2) High-magnification image of box in (b1). (b3) Overlapped Mg+ Al+ Si mapping image. Alumina-depleted post-perovskite (PPv, purple) and hydrous δ-phase (green) coexist. (b4) Mg mapping image, (b5) Al mapping image, and (b6) Si mapping image.

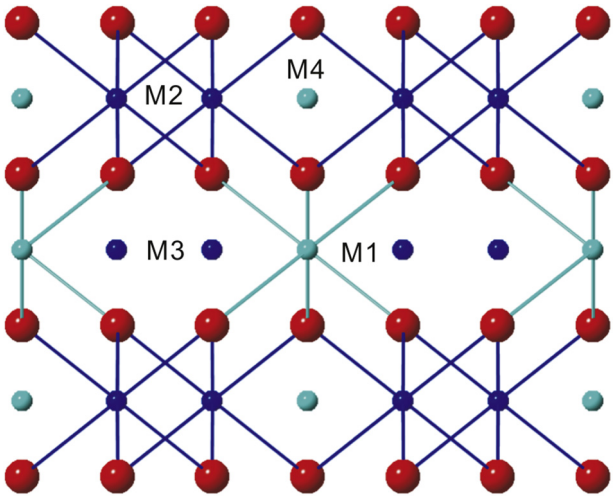

Fig. 9. The structure of Al phase D [50]. Al phase D has a structure corresponding to hexagonal space group $P6_3/mcm$, shown here projected down the *a* axis. The octahedral sites are named according to the structure of Mg-phase D in trigonal space group $P\bar{3}1m$. In the Mg endmember, Mg and Si exclusively occupy M1 and M2 sites respectively, with M3 and M4 sites vacant. In pure Al-phase D M1 and M4 sites are equivalent, the same as M2 and M3 sites. All six octahedral sites are partially occupied by a random distribution of Si and Al.

Accordingly, essentially undistorted octahedral in Al-phase D gave rise to much higher thermal stability, compared to that of Mg-phase D with strongly distorted octahedra. On the basis of these results, researchers proposed that the deep water could be dominantly stored in such Al-rich hydrous silicates, which can be formed within the mafic parts of the subducting slab via the migration of hydrous melt released from their Al-poor counterparts [50]. Further in-situ study on Al-rich phase at high $P-T$ is needed to examine structure-stability relation extending to deep lower mantle conditions.

4. Crystal structure of minerals and oxidation state in the deep lower mantle

In geological research, the term “oxidation state” has two different meanings: the valence state of elements and the chemical potential of oxygen (referred as oxygen fugacity) [60]. Our limited knowledge of oxygen fugacity in deep Earth is derived from the basis of precious few samples of the lower mantle [60]. Here we present examples on the relationship between mineral crystal structure and oxidation state, indicative of the possibly heterogeneous oxygen fugacity in the deep lower mantle.

4.1. Incorporation of Fe^{3+} into Al-bearing bridgmanite

The lower mantle is believed to contain a small amount of Al. McCammon performed a Mössbauer study of Al-free and Al-bearing (Mg, Fe)SiO_3 bridgmanite to determine the Fe oxidation state [61]. Natural orthopyroxene from San Carlos, Arizona was treated at 25 GPa and 1600 °C for 2 h using the multi-anvil press to prepare the Al-bearing (Mg, Fe)SiO_3 bridgmanite containing 3.3 wt.% Al_2O_3. Al-free $Mg_{0.94}Fe_{0.06}SiO_3$ bridgmanite was synthesized from synthetic orthopyroxene in the multi-anvil press at 24 GPa and 1650 °C for 30 min. The room-temperature Mössbauer spectra showed that the ferric iron content $Fe^{3+}/\sum Fe$ in Al-free (Mg, Fe)SiO_3 bridgmanite was 16 ± 3%, while the $Fe^{3+}/\sum Fe$ value in Al-bearing (Mg, Fe)SiO_3 bridgmanite was 50 ± 5% [61]. Subsequent studies by McCammon et al. showed that (Mg, Fe, Al)(Si, Al)O_3 pyroxene compositions (believed to have been originally in the bridgmanite structure) in diamonds from São Luiz, Brazil, contained high relative amount of Fe^{3+} ($Fe^{3+}/\sum Fe = 20\% - 70\%$) [62].

Frost et al. synthesized samples of Al-bearing (Mg, Fe)SiO_3 bridgmanite coexisting with metallic Fe to determine the Fe^{3+}/

Please cite this article in press as: H. Yuan, L. Zhang, In situ determination of crystal structure and chemistry of minerals at Earth's deep lower mantle conditions, Matter and Radiation at Extremes (2017), http://dx.doi.org/10.1016/j.mre.2017.01.002

∑Fe ratio of bridgmanite under these extremely reducing conditions [63]. Furthermore, experiments without additional metallic Fe were performed using a synthetic peridotite composition under conditions around the silicate solidus. The $Fe^{3+}/\sum Fe$ ratios of Al-bearing (Mg, Fe)SiO_3 bridgmanite in the recovered samples were measured using Mössbauer and electron energy loss spectroscopy (see Fig. 10). High Fe^{3+} concentrations from 35% to 68% could be found in the recovered Al-bearing (Mg, Fe)SiO_3 bridgmanite [63]. Fe^{3+} content of bridgmanite was coupled with Al^{3+} concentration in a nonlinear relationship, probably because the dominant trivalent cation incorporation involving oxygen vacancies at low Al^{3+} concentrations changed to a coupled substitution of trivalent cations at higher Al^{3+} concentrations [63]. Experiments performed above the silicate solidus also demonstrated that bridgmanite had a significant Fe^{3+} concentration during either crystallization or partial melting [63]. The above results suggested that the combined Al^{3+} and iron substitution into magnesium silicate bridgmanite stabilized Fe^{3+}, even under extremely reducing conditions.

Detailed information of crystal chemistry of Al, Fe-bearing bridgmanite is essential for understanding the dominant component in the lower mantle. However, in-situ single-crystal studies of bridgmanite under high pressure have been limited to the multianvil-synthesized single-crystal bridgmanite samples in a DAC [64]. Multigrain crystallography has enabled in situ single-crystal structure determination under phase

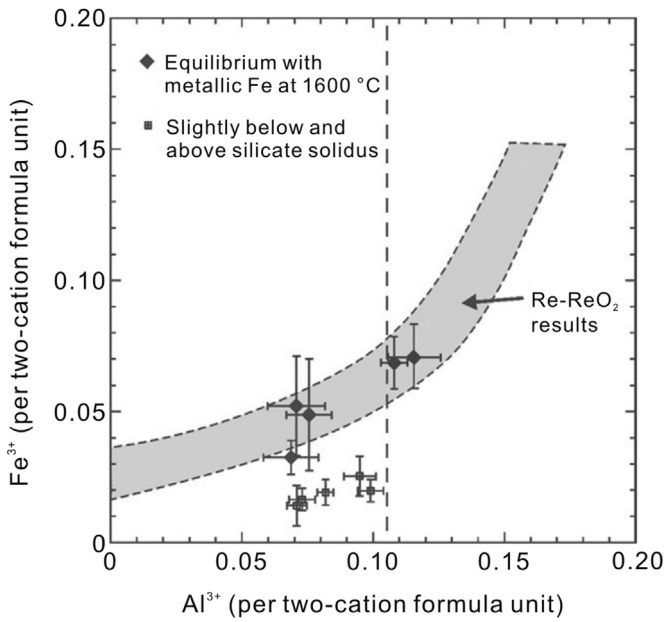

Fig. 10. The variation of Al^{3+} and Fe^{3+} in Al-bearing (Mg, Fe)SiO_3 bridgmanite reported as atoms per two-cation formula unit. Analyses from experiments performed in equilibrium with metallic Fe at a typical temperature for the top of the lower mantle (1600 °C) are shown as black diamonds [63]. The gray field encompasses analyses from experiments performed at a higher oxygen fugacity in equilibrium with the Re–ReO_2 buffer. Analyses of bridgmanites forming slightly below and above the silicate solidus (~2200 °C) are shown as small squares. The vertical dotted line indicates the approximate Al content of silicate bridgmanite expected in a lower mantle with a typical bulk silicate earth composition.

equilibrium conditions extending to powder starting samples with variable compositions to Mbar pressure range. Future research should focus on in situ single-crystal structural analysis to understand the detailed crystal chemistry of bridgmanite under realistic lower mantle chemistry (including Al^{3+}, Fe^{2+}, Fe^{3+}, and H_2O).

4.2. Synthesis of FeO_2 under oxidizing conditions

Iron, the Earth's most abundant element by mass, can adopt multiple oxidation states, i.e., 3+, 2+, and 0 in the oxide mantle. The extreme P–T conditions of the Earth's deep interior fundamentally alter the oxidation states, spin states, and phase stabilities of the iron–oxygen binary system, creating new stoichiometries, such as Fe_4O_5 [65], Fe_5O_6 [66] and $Fe_{13}O_{19}$ [67]. Recently, Hu et al. reported the synthesis of FeO_2 by redox reaction between Fe_2O_3 and O_2 as well as a decomposition reaction of FeOOH under deep lower mantle conditions [68].

The dehydrated α-Fe_2O_3 (hematite) powder sample was pre-compressed into a disk of ~10 μm thickness cut to ~60 μm in diameter, and then placed in a ~100 μm diameter Re gasket hole in a Mao-type symmetric DAC with the culet size of 200 μm to access pressures above 70 GPa [68]. Condensed liquid O_2 was loaded in the sample chamber as both oxidant and pressure media. At lower pressures, the pressure was calibrated by ruby fluorescence [68]. At higher pressures, since ruby fluorescence modes were hard to detect, the lowest derivative value of diamond Raman peak was taken as additional calibration. The pressure was initially raised to 78 GPa; no reaction between hematite and oxygen was observed at ambient temperature. After the laser heating the sample at 1800 K at high pressure, the sample turned into semi-transparent (see Fig. 11(b)), suggesting a chemical reaction. The as-obtain XRD pattern was very speckled (see Fig. 11(a)), which was ideal for the aforementioned multigrain crystallography method [68]. The "rotation method" was applied to collect the data for processing multigrain crystallography analysis. Five single crystals were selected for single-crystal analysis, and the results showed that the new-found phase was FeO_2 (referred as P-phase), adopting the space group of $Pa\bar{3}$ identical to FeS_2 (pyrite) with oxygen replacing sulfur. Analogous to the archetypical pyrite and peroxides, iron in FeO_2 was considered to be ferrous. For the structure of P-phase, oxygen atoms not only formed O–Fe bonds of 1.792 Å in length but also formed O–O bonds of 1.937 Å in length. Interestingly, the oxidation of Fe_2O_3 to FeO_2 reduced Fe^{3+} to Fe^{2+}. This can be understood with the concurrent oxidation of O^{2-} partially to O^0 as indicated by the O–O bond in the phase. The reaction $2Fe_2O_3 + O_2 = 4FeO_2$ is a paradigm of how structure-chemistry constrains make the Fe^{2+} fully occupied in the Fe–O join, even under extremely oxidizing conditions [68].

For α-FeOOH (goethite), a pre-compressed thin disk was cut to ~35 μm in diameter and then placed in a ~95 μm diameter Re gasket hole in a Mao-type symmetric DAC with the culet size of 150 μm to access pressures above 92 GPa.

Please cite this article in press as: H. Yuan, L. Zhang, In situ determination of crystal structure and chemistry of minerals at Earth's deep lower mantle conditions, Matter and Radiation at Extremes (2017), http://dx.doi.org/10.1016/j.mre.2017.01.002

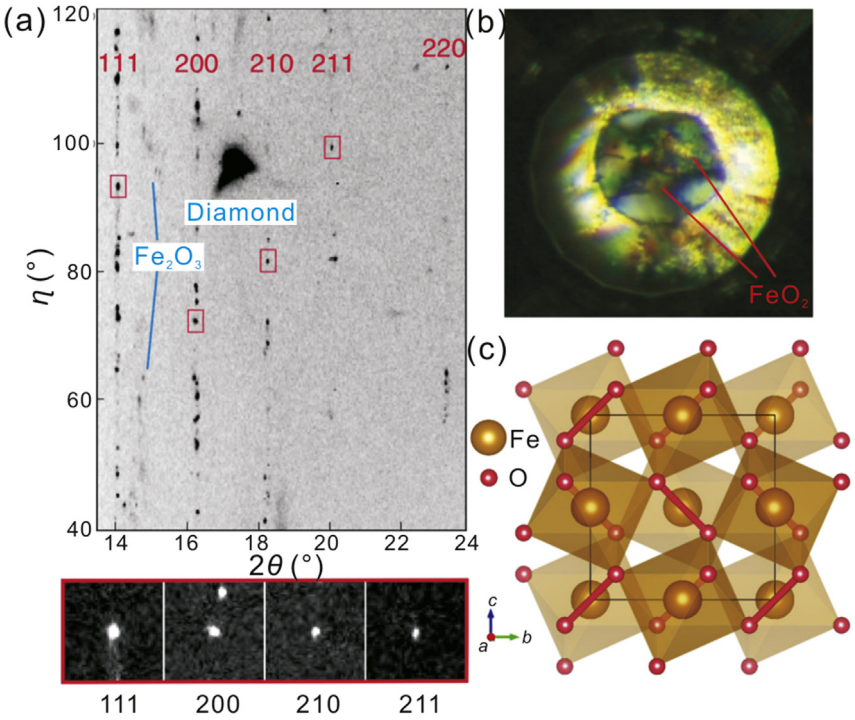

Fig. 11. (a) 2D XRD image of the $Fe_2O_3 + O_2$ experiment at 76 GPa after laser-heating pattern integrated along collected at $\omega = -8.5°$, with X-ray wavelength of 0.6199 Å. The original image in 2θ-η polar coordination is converted into Cartisian coordination ("caked") for clarity. The newly developed sharp spots are attributed to multiple single crystals of FeO_2, while smeared powder rings are from the remaining Fe_2O_3. Four selected diffraction spots and their miller indexes from P-phase single crystallites are shown in the lower panel. (b) Microphotographic image of FeO_2 under pressure through diamond culets. (c) Structural representation of pyrite-type FeO_2 [68].

Compressed Ne was loaded as the pressure medium and pressure standard before heating. After heating the sample up to 2000 K at 92 GPa, the XRD patterns clearly showed the conversion of goethite to P-phase (see Fig. 12), indicating the reaction: $2FeOOH = 2FeO_2 + H_2$. Raman spectroscopy was used to verify H_2 Raman vibration mode, which peaked at 5180 cm^{-1} in Ne medium. The production of free H_2 indicated a moderately reducing condition for the formation of the P-

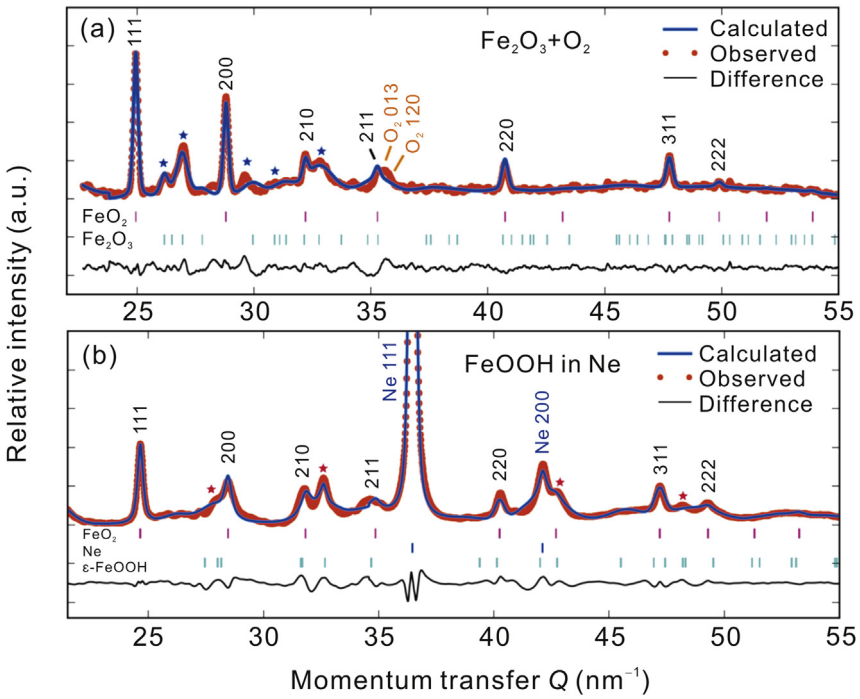

Fig. 12. Integrated XRD pattern and *Rietveld* refinement of the pyrite-type FeO_2 phase [68]. (a) FeO_2 synthesized from Fe_2O_3 and O_2 at 76 GPa, $R_p = 0.0022$, $wR_p = 0.0031$. Blue stars belong to residual Rh_2O_3-type Fe_2O_3. (b) FeO_2 synthesized from FeOOH at 87 GPa, $R_p = 0.0032$, $wR_p = 0.0052$. Red stars belong to residual ε-FeOOH.

Please cite this article in press as: H. Yuan, L. Zhang, In situ determination of crystal structure and chemistry of minerals at Earth's deep lower mantle conditions, Matter and Radiation at Extremes (2017), http://dx.doi.org/10.1016/j.mre.2017.01.002

phase. First-principle calculations also predicted the P-phase to be stable at 100–465 GPa. The experimentally observed structural parameters of P-phase FeO_2 were in excellent agreement with the *ab-initio* prediction. The decomposition reaction of FeOOH might cause accumulation of the heavy FeO_2-bearing patches in the deep lower mantle, upward migration of the hydrogen, and separation of the oxygen and hydrogen cycles. And the P-phase assemblages might account for many unexplained seismic and geochemical anomalies in the deep lower mantle down to the D″ layer [68].

5. Conclusions

Powder diffraction has been the dominant tool for petrological and mineralogical studies at Earth's lower mantle $P-T$ conditions. Introducing multigrain method into high pressure research has opened a new area of high-pressure single-crystal crystallography, especially in a multiphase assemblage [69]. On the other hand, ex situ TEM-EDX analysis can provide direct compositional information from recovered samples to ambient conditions [4,38–41]. These advanced techniques have enabled studies of mineral crystal structure and chemistry under Earth's lower mantle $P-T$ conditions. Using advanced techniques, intriguing properties of lower mantle minerals have been discovered, providing mineralogical mechanisms for chemical heterogeneities and seismic discontinuities within the lowermost mantle.

Acknowledgments

The authors acknowledge the support from the Foundation of President of China Academy of Engineering Physics (Grant No: 201402032) and National Natural Science Foundation of China (Grant No: 41574080 and U1530402).

References

[1] A.M. Dziewonski, D.L. Anderson, Preliminary reference Earth model, Phys. Earth Planet. Inter. 25 (4) (1981) 297–356.
[2] W.F. McDonough, S.S. Sun, The composition of the Earth, Chem. Geol. 120 (3–4) (1995) 223–253.
[3] L. Zhang, Y. Meng, P. Dera, W. Yang, W.L. Ma, et al., Single-crystal structure determination of (Mg, Fe) SiO_3 postperovskite, Proc. Natl. Acad. Sci. 110 (16) (2013) 6292–6295.
[4] L. Zhang, Y. Meng, W. Yang, L. Wang, W.L. Mao, et al., Disproportionation of (Mg, Fe) SiO_3 perovskite in Earth's deep lower mantle, Science 344 (6186) (2014) 877–882.
[5] R.D. van der Hilst, M.V. de Hoop, P. Wang, S.H. Shim, P. Ma, et al., Seismostratigraphy and thermal structure of Earth's core-mantle boundary region, Science 315 (5820) (2007) 1813–1817.
[6] K. Hirose, Postperovskite phase transition and its geophysical implications, Rev. Geophys. 44 (3) (2006) RG3001.
[7] S.H. Shim, The postperovskite transition, Annu. Rev. Earth Planet. Sci. 36 (12) (2008) 569–599.
[8] I. Sidorin, M. Gurnis, D.V. Helmberger, Discontinuity at the base of the mantle, Science 286 (5443) (1999) 1326–1331.
[9] M. Murakami, K. Hirose, K. Kawamura, N. Sata, Y. Ohishi, Post-perovskite phase transition in $MgSiO_3$, Science 304 (5672) (2004) 855–858.
[10] S.-H. Shim, T. Lay, Post-perovskite at ten, Nat. Geosci. 7 (9) (2014) 621–623.
[11] A.R. Oganov, S. Ono, Theoretical and experimental evidence for a post-perovskite phase of $MgSiO_3$ in Earth's D' layer, Nature 430 (6998) (2004) 445–448.
[12] T. Tsuchiya, J. Tsuchiya, K. Umemoto, R.M. Wentzcovitch, Phase transition in $MgSiO_3$ perovskite in the earth's lower mantle, Earth Planet. Sci. Lett. 224 (3–4) (2004) 241–248.
[13] D.R. Hummer, Y. Fei, Synthesis and crystal chemistry of Fe^{3+}-bearing $(Mg,Fe^{3+})(Si,Fe^{3+})O_3$ perovskite, Am. Mineral. 97 (11–12) (2012) 1915–1921.
[14] T.B. Ballaran, A. Kurnosov, K. Glazyrin, D.J. Frost, M. Merlini, et al., Effect of chemistry on the compressibility of silicate perovskite in the lower mantle, Earth Planet. Sci. Lett. 333–334 (2012) 181–190.
[15] J.-F. Lin, Z. Mao, J. Yang, J. Liu, Y. Xiao, et al., High-spin Fe^{2+} and Fe^{3+} in single-crystal aluminous bridgmanite in the lower mantle, Geophys. Res. Lett. 43 (13) (2016), 2016GL069836.
[16] M. Dorfman Susannah, J. Badro, P. Rueff, P. Chow, Y. Xiao, et al., Composition dependence of spin transition in $(Mg,Fe)SiO_3$ bridgmanite, Am. Mineral. 100 (2015) 2246.
[17] T. Okuchi, N. Purevjav, N. Tomioka, J.-F. Lin, T. Kuribayashi, et al., Synthesis of large and homogeneous single crystals of water-bearing minerals by slow cooling at deep-mantle pressures, Am. Mineral. 100 (2015) 1483.
[18] L. Ismailova, E. Bykova, M. Bykov, V. Cerantola, C. McCammon, et al., Stability of Fe, Al-bearing bridgmanite in the lower mantle and synthesis of pure Fe-bridgmanite, Sci. Adv. 2 (7) (2016) e1600427.
[19] W.L. Mao, H.k. Mao, V.B. Prakapenka, J. Shu, R.J. Hemley, The effect of pressure on the structure and volume of ferromagnesian post-perovskite, Geophys. Res. Lett. 33 (12) (2006).
[20] S.R. Shieh, T.S. Duffy, A. Kubo, G. Shen, V.B. Prakapenka, et al., Equation of state of the postperovskite phase synthesized from a natural $(Mg,Fe)SiO_3$ orthopyroxene, Proc. Natl. Acad. Sci. U.S.A. 103 (9) (2006) 3039–3043.
[21] S.-H. Shim, K. Catalli, J. Hustoft, A. Kubo, V.B. Prakapenka, et al., Crystal structure and thermoelastic properties of $(Mg_{0.91}Fe_{0.09})SiO_3$ postperovskite up to 135 GPa and 2,700 K, Proc. Natl. Acad. Sci. 105 (21) (2008) 7382–7386.
[22] T. Lay, E.J. Garnero, Reconciling the post-perovskite phase with seismological observations of lowermost mantle structure, in: Post-Perovskite: The Last Mantle Phase Transition, American Geophysical Union, 2013, pp. 129–153.
[23] T. Lay, Sharpness of the D" discontinuity beneath the Cocos Plate: implications for the perovskite to post-perovskite phase transition, Geophys. Res. Lett. 35 (3) (2008) L03304.
[24] M.E. Wysession, T. Lay, J. Revenaugh, Q. Williams, E.J. Garnero, et al., The D" discontinuity and its implications, in: The Core-Mantle Boundary Region, American Geophysical Union, 2013, pp. 273–297.
[25] K. Catalli, S.-H. Shim, V. Prakapenka, Thickness and Clapeyron slope of the post-perovskite boundary, Nature 462 (7274) (2009) 782–785.
[26] W.L. Mao, Y. Meng, G. Shen, V.B. Prakapenka, A.J. Campbell, et al., Iron-rich silicates in the Earth's D" layer, Proc. Natl. Acad. Sci. U. S. A. 102 (28) (2005) 9751–9753.
[27] W.L. Mao, H.-K. Mao, W. Sturhahn, J. Zhao, V.B. Prakapenka, et al., Iron-rich post-perovskite and the origin of ultralow-velocity zones, Science 312 (5773) (2006) 564–565.
[28] T. Yamanaka, K. Hirose, W.L. Mao, Y. Meng, P. Ganesh, et al., Crystal structures of (Mg_{1-x}, Fe_x) SiO_3 postperovskite at high pressures, Proc. Natl. Acad. Sci. 109 (4) (2012) 1035–1040.
[29] H.O. Sørensen, S. Schmidt, J.P. Wright, G. Vaughan, S. Techert, et al., Multigrain crystallography, Z. für Kristallogr. Cryst. Mater. 227 (1) (2012) 63–78.
[30] Y. Fei, A. Ricolleau, M. Frank, K. Mibe, G. Shen, et al., Toward an internally consistent pressure scale, Proc. Natl. Acad. Sci. 104 (22) (2007) 9182–9186.
[31] A. Dewaele, P. Loubeyre, M. Mezouar, Equations of state of six metals above 94 GPa, Phys. Rev. B 70 (9) (2004) 094112.
[32] S. Schmidt, GrainSpotter: a fast and robust polycrystalline indexing algorithm, J. Appl. Crystallogr. 47 (1) (2014) 276–284.

Please cite this article in press as: H. Yuan, L. Zhang, In situ determination of crystal structure and chemistry of minerals at Earth's deep lower mantle conditions, Matter and Radiation at Extremes (2017), http://dx.doi.org/10.1016/j.mre.2017.01.002

[33] P. Dera, GSE-ADA Data Analysis Program for Monochromatic Single Crystal Diffraction with Area Detector, GeoSoilEnviroCARS, Argonne, Illinois, 2007.
[34] G.M. Sheldrick, A short history of SHELX, Acta Crystallogr. Sect. A Found. Crystallogr. 64 (1) (2008) 112–122.
[35] Y. Fei, H.K. Mao, B.O. Mysen, Experimental determination of element partitioning and calculation of phase relations in the MgO-FeO-SiO_2 system at high pressure and high temperature, J. Geophys. Res. Solid Earth 96 (B2) (1991) 2157–2169.
[36] J. Li, V.V. Struzhkin, H.-K. Mao, J. Shu, R.J. Hemley, et al., Electronic spin state of iron in lower mantle perovskite, Proc. Natl. Acad. Sci. U. S. A. 101 (39) (2004) 14027–14030.
[37] M. Jackson Jennifer, W. Sturhahn, G. Shen, J. Zhao, Y. Hu Michael, et al., A synchrotron Mössbauer spectroscopy study of (Mg,Fe)SiO_3 perovskite up to 120 GPa, Am. Mineral. 90 (2005) 199.
[38] T. Irifune, M. Isshiki, S. Sakamoto, Transmission electron microscope observation of the high-pressure form of magnesite retrieved from laser heated diamond anvil cell, Earth Planet. Sci. Lett. 239 (1–2) (2005) 98–105.
[39] A.-L. Auzende, J. Badro, F.J. Ryerson, P.K. Weber, S.J. Fallon, et al., Element partitioning between magnesium silicate perovskite and ferropericlase: new insights into bulk lower-mantle geochemistry, Earth Planet. Sci. Lett. 269 (1–2) (2008) 164–174.
[40] M. Miyahara, T. Sakai, E. Ohtani, Y. Kobayashi, S. Kamada, et al., Application of FIB system to ultra-high-pressure Earth science, J. Mineral. Petrol. Sci. 103 (2) (2008) 88–93.
[41] A. Ricolleau, G. Fiquet, A. Addad, N. Menguy, C. Vanni, et al., Analytical transmission electron microscopy study of a natural MORB sample assemblage transformed at high pressure and high temperature, Am. Mineral. 93 (2008) 144.
[42] E. Ohtani, Hydrous minerals and the storage of water in the deep mantle, Chem. Geol. 418 (2015) 6–15.
[43] D. Pearson, F. Brenker, F. Nestola, J. McNeill, L. Nasdala, et al., Hydrous mantle transition zone indicated by ringwoodite included within diamond, Nature 507 (7491) (2014) 221–224.
[44] R. Van der Hilst, S. Widiyantoro, E. Engdahl, Evidence for deep mantle circulation from global tomography, Nature 386 (1997) 578–584.
[45] A. Ringwood, A. Major, High-pressure reconnaissance investigations in the system Mg_2SiO_4-MgO-H_2O, Earth Planet. Sci. Lett. 2 (2) (1967) 130–133.
[46] L.-g. Liu, Effects of H_2O on the phase behaviour of the forsterite-enstatite system at high pressures and temperatures and implications for the Earth, Phys. Earth Planet. Inter. 49 (1–2) (1987) 142–167.
[47] M. Nishi, T. Irifune, J. Tsuchiya, Y. Tange, Y. Nishihara, et al., Stability of hydrous silicate at high pressures and water transport to the deep lower mantle, Nat. Geosci. 7 (3) (2014) 224–227.
[48] E. Ohtani, Y. Amaike, S. Kamada, T. Sakamaki, N. Hirao, Stability of hydrous phase H $MgSiO_4H_2$ under lower mantle conditions, Geophys. Res. Lett. 41 (23) (2014) 8283–8287.
[49] I. Ohira, E. Ohtani, T. Sakai, M. Miyahara, N. Hirao, et al., Stability of a hydrous δ-phase, AlOOH–$MgSiO_2(OH)_2$, and a mechanism for water transport into the base of lower mantle, Earth Planet. Sci. Lett. 401 (2014) 12–17.
[50] M.G. Pamato, R. Myhill, T.B. Ballaran, D.J. Frost, F. Heidelbach, et al., Lower-mantle water reservoir implied by the extreme stability of a hydrous aluminosilicate, Nat. Geosci. 8 (1) (2015) 75–79.
[51] J. Tsuchiya, First principles prediction of a new high-pressure phase of dense hydrous magnesium silicates in the lower mantle, Geophys. Res. Lett. 40 (17) (2013) 4570–4573.
[52] K. Komatsu, A. Sano-Furukawa, H. Kagi, Effects of Mg and Si ions on the symmetry of δ-AlOOH, Phys. Chem. Miner. 38 (9) (2011) 727–733.
[53] T. Kuribayashi, A. Sano-Furukawa, T. Nagase, Observation of pressure-induced phase transition of δ-AlOOH by using single-crystal synchrotron X-ray diffraction method, Phys. Chem. Miner. 41 (4) (2014) 303–312.
[54] J. Tsuchiya, T. Tsuchiya, S. Tsuneyuki, T. Yamanaka, First principles calculation of a high-pressure hydrous phase, δ-AlOOH, Geophys. Res. Lett. 29 (19) (2002) 1909.
[55] W.R. Panero, L.P. Stixrude, Hydrogen incorporation in stishovite at high pressure and symmetric hydrogen bonding in δ-AlOOH, Earth Planet. Sci. Lett. 221 (1–4) (2004) 421–431.
[56] S. Li, R. Ahuja, B. Johansson, The elastic and optical properties of the high-pressure hydrous phase δ-AlOOH, Solid State Commun. 137 (1–2) (2006) 101–106.
[57] X. Xue, M. Kanzaki, H. Fukui, E. Ito, T. Hashimoto, Cation order and hydrogen bonding of high-pressure phases in the Al_2O_3-SiO_2-H_2O system: an NMR and Raman study, Am. Mineral. 91 (2006) 850.
[58] E. Ohtani, K. Litasov, A. Suzuki, T. Kondo, Stability field of new hydrous phase, δ-AlOOH, with implications for water transport into the deep mantle, Geophys. Res. Lett. 28 (20) (2001) 3991–3993.
[59] E. Ohtani, K. Litasov, T. Hosoya, T. Kubo, T. Kondo, Water transport into the deep mantle and formation of a hydrous transition zone, Phys. Earth Planet. Inter. 143 (2004) 255–269.
[60] C. McCammon, The paradox of mantle redox, Science 308 (5723) (2005) 807–808.
[61] C. McCammon, Perovskite as a possible sink for ferric iron in the lower mantle, Nature 387 (6634) (1997) 694–696.
[62] C. McCammon, M. Hutchison, J. Harris, Ferric iron content of mineral inclusions in diamonds from Sao Luiz: a view into the lower mantle, Science 278 (5337) (1997) 434–436.
[63] D.J. Frost, C. Liebske, F. Langenhorst, C.A. McCammon, R.G. Tronnes, et al., Experimental evidence for the existence of iron-rich metal in the Earth's lower mantle, Nature 428 (6981) (2004) 409–412.
[64] L. Dubrovinsky, T. Boffa-Ballaran, K. Glazyrin, A. Kurnosov, D. Frost, et al., Single-crystal X-ray diffraction at megabar pressures and temperatures of thousands of degrees, High Press. Res. 30 (4) (2010) 620–633.
[65] B. Lavina, P. Dera, E. Kim, Y. Meng, R.T. Downs, et al., Discovery of the recoverable high-pressure iron oxide Fe_4O_5, Proc. Natl. Acad. Sci. 108 (42) (2011) 17281–17285.
[66] B. Lavina, Y. Meng, Synthesis of Fe_5O_6, Sci. Adv. 1 (5) (2015) e1400260.
[67] M. Merlini, M. Hanfland, A. Salamat, S. Petitgirard, H. Müller, The crystal structures of $Mg_2Fe_2C_4O_{13}$, with tetrahedrally coordinated carbon, and $Fe_{13}O_{19}$, synthesized at deep mantle conditions, Am. Mineral. 100 (8–9) (2015) 2001–2004.
[68] Q. Hu, D.Y. Kim, W. Yang, L. Yang, Y. Meng, et al., FeO_2 and FeOOH under deep lower-mantle conditions and Earth's oxygen–hydrogen cycles, Nature 534 (7606) (2016) 241–244.
[69] L. Zhang, Y. Meng, H.-K. Mao, Unit cell determination of coexisting post-perovskite and H-phase in (Mg,Fe)SiO_3 using multigrain XRD: compositional variation across a laser heating spot at 119 GPa, Prog. Earth Planet. Sci. 3 (1) (2016) 1–6.
[70] S. Ono, T. Kikegawa, Y. Ohishi, Equation of state of $CaIrO_3$-type $MgSiO_3$ up to 144 GPa, Am. Mineral. 91 (2006) 475.

Please cite this article in press as: H. Yuan, L. Zhang, In situ determination of crystal structure and chemistry of minerals at Earth's deep lower mantle conditions, Matter and Radiation at Extremes (2017), http://dx.doi.org/10.1016/j.mre.2017.01.002